



Measurement of weld depressions in thin-walled steel tubes before and after circumferential welding

Dehui Lin¹, Anil Pervizaj², Søren Bøgelund Madsen³, Andrew T. Myers⁴

Abstract

Thin-walled circular steel tubes are a widely-used structural element for wind turbine towers. An important limit state for these tubes is local buckling of the tube wall in compression and the strength of this limit state is sensitive to geometric imperfections, which are sensitive to the fabrication process. Wind turbine tower sections are usually manufactured by can-welding, where flat steel plates are rolled into cylinders and seam-welded into “cans,” fit to adjacent cans by tack welding along the circumference between cans, and fully connected with a continuous circumferential weld. A well-known imperfection induced by this process is the weld depression, a radially inward axisymmetric deviation formed during the cooling of the circumferential weld. These depressions have an important influence on the structural behavior of thin-walled tubes, so it is meaningful to understand the evolution of this imperfection pattern during the fabrication process. Using the latest noncontact laser-scanning instrumentation, full-field measurements are used in this paper to capture the change in geometric imperfections of two can-welded tubes before and after full circumferential welding. The two tube sections have diameter D equal to 1003 mm and thickness t equal to 4.8 mm, corresponding to a diameter-to-thickness ratio D/t equal to 211. These tubes are roughly a 1:4 scale model of a wind turbine tower section. Geometric imperfections of these tubes, defined as radial deviations between the measured geometry and the nominal geometry based on drawings, are presented and compared. Weld depression profiles of the measured geometry before and after circumferential welding are isolated and compared.

1. Introduction

Thin-walled circular steel tube sections, like all fabricated structural elements, experience deviations of shape and form from their ideal geometric profile. Such deviations are called geometric imperfections, which inevitably arise from the manufacturing process and are influenced by how the sections are fabricated. An important limit state for the design of wind turbine tower sections is local buckling of the tube wall when loaded in compression and this limit state is sensitive to geometric imperfections, so characterizing these geometric imperfections has important design implications.

¹ Ph.D. Candidate, Northeastern University, <lin.deh@northeastern.edu>

² Lead Engineer, Vestas Wind Systems A/S, <anpij@vestas.com >

³ Structural Specialist, Vestas Wind Systems A/S, <sobgm@vestas.com >

⁴ Associate Professor, Northeastern University, USA <an.myers@northeastern.edu>

Wind turbine tower sections are usually manufactured using a process called “can-welding”, where flat steel plates are rolled into cylinders and seam-welded into “cans,” fit to adjacent cans by tack welding along the circumference between cans, and fully connected with a continuous circumferential weld. A well-known imperfection induced by this process is a “weld depression,” wherein material around the circumferential welds is exposed to large temperature changes during the welding and cooling processes. During these processes, the material near the circumferential welds shortens circumferentially, acting like a belt cinching around the tube and generating a radially inward axisymmetric deviation.

Weld depressions have been shown by researchers to be important for understanding the structural behavior of thin-walled tubes (Rotter et al. 1989), and it is meaningful to understand the evolution of this imperfection pattern during the fabrication process. Recent advances in 3D laser scanning technology make it viable to accurately measure the full-field of this imperfection pattern. The goal of this paper is to study the evolution of geometric imperfections of two thin-walled tube sections before and after circumferential welding using 3D full-field measurement data with a laser scanner to understand how the profile of the weld depression evolves during the circumferential welding process.

This paper is organized as follows. First, background information on weld depression profiles is reviewed, along with measurements in the literature of geometric imperfections in steel structural components. Next, the methodology for obtaining scanning measurements and processing them to extract imperfections is described. Then, the imperfection data processed from the measurements is used to isolate and analyze weld depression profiles of the sections before and after circumferential welding. Finally, conclusions of the study are provided.

2. Background

2.1 Theoretical model of weld depression profile

Researchers have proposed various theoretical or empirical models for the imperfection profile associated with circumferential welds (White et al. 1997, Pircher et al. 2001). The model proposed by Rotter and Teng (Rotter et al. 1989) is widely used and is noted as a particularly damaging imperfection pattern for thin cylindrical shells under uniform axial compression and global bending (Sadowski et al. 2015).

Rotter and Teng derived a formula for the weld depression profile considering two idealized extreme situations. In both cases, the circumferential weld is assumed to impose a radially inward force on the tube during cooling and the resulting deformation follows that of a beam on an elastic foundation. In one extreme, the weld is assumed to act like a fully continuous moment connection. This assumption generates a smooth weld depression shape with zero slope at the centerline. In the other extreme, the weld is assumed to act like a hinge, transferring no moments, across the circumferential weld. This assumption generates a pointed profile, with a discontinuous slope at the centerline. In fabricated tubes, the degree of moment continuity across the circumferential weld varies between these two extremes, which are both represented by Eq. 1:

$$w_{weld\ induced}(x) = w_0 e^{\frac{\pi|x-x_w|}{\lambda}} \left[\cos\left(\frac{\pi|x-x_w|}{\lambda}\right) + \xi \sin\left(\frac{\pi|x-x_w|}{\lambda}\right) \right] \quad (1)$$

where x is the longitudinal position along the length of the tube, x_w represents the location of the weld centerline, w_0 is the weld depression magnitude at the weld centerline, λ represents the half-wavelength of the depression, and ξ represents the rotational stiffness of the connection across circumferential weld and can vary between 0 and 1. Profiles of the R&T model, corresponding to $\xi = 0$ and 1, are illustrated in Fig.1.

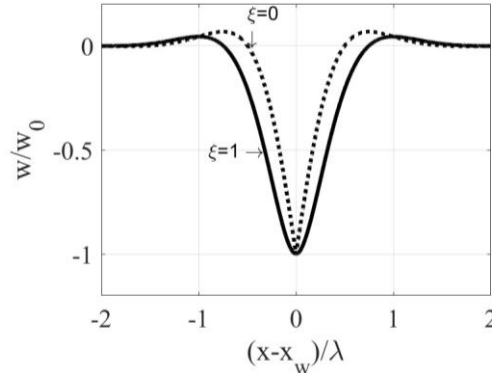


Fig 1: A typical R&T weld depression profile for $\xi = 0$ (no moment transfer across the weld) and $\xi = 1$ (moment transfer across the weld).

2.2 Measurements of geometric imperfections using 3D laser scanning technology

This paper uses a tripod-mounted Artec Ray 3D scanner to measure geometric imperfections of thin-walled tubes. The scanning device has an angular accuracy of 25 arcsecs, a recommended working range of up to 50m, and a scanning speed of 208,0000 points/sec. It works by continuously emitting laser pulses into different directions (360° horizontally and 270° vertically), and upon contact with an object, a laser pulse reflects back to the scanner to generate the 3D coordinates of measurement point. This process is repeated until a sufficiently resolved 3D point cloud of the data is recorded.

For the size of the tubes considered here, full-field point clouds of the tubes are generated by scanning the tubes multiple times from different locations, all external to the tube. There are several factors to consider when selecting the number of scans required, including the viewing range of the scanner (e.g., a scanner placed on the left side of the tube fails to scan the right side of the tube), the incident angle, and the distance between the scanner and the object. Among these, the incident angle (i.e., the angle between incoming laser and the surface normal) is an especially sensitive factor because it influences the noise of the scan to a large extent (Soudarissanane et al. 2011). The literature has varying criteria on the maximum allowable incident angle, but it's usually between $60^\circ \sim 70^\circ$ (Lichti 2007). Based on previous experience with the scanner used here, the incidence angle for the measurement campaign described here was limited to 70° to remove non-reliable data when exporting data from the scanner. After scanning, datasets from each scanning position are merged by a process referred to as either registration or alignment. The registration process uses a reference target set that is located within the overlapping scanning area of two adjacent scans during scanning (Guo et al. 2020).

Once the measured geometry of the specimen is obtained, a reference “ideal” geometry is established for calculation of geometric imperfections (i.e., deviations from the “ideal geometry”). A reference geometry can be the nominal geometry of the structural component based on drawings

(Selvaraj et al. 2018), or a best-fit geometric feature to match the measured geometry, e.g., a best-fit cylinder for a pipeline (Kainat 2012) or a best-fit cone for tower sections (Mirzaie 2020). In this study, the nominal geometry specified in the drawings is used as the reference geometry.

The alignment between the measured geometry and the reference geometry is usually achieved using the “Iterative Closest Point” (ICP) method, which is an algorithm to align two point clouds by minimizing the sum of the square of distances between corresponding points (Wang et al. 2017). After that, geometric imperfections can be calculated. For this study, geometric imperfections are defined as the radial deviation between the measured geometry and the reference geometry, where the direction of the radius is determined from the reference geometry.

3. Scan data acquisition

Two tube sections which are approximately $\frac{1}{4}$ the size of full-scale wind tower sections are studied. These sections, with identical geometric and material properties (i.e., material, radius, length, thickness), are referred to as “Section-A” and “Section-B”, respectively, and their complete geometric profiles are analyzed using measurements from a 3D laser scanner, before and after circumferential welding between cans. As shown in Fig.2, each tube section includes 5 steel cylinders with equal thicknesses, three full lengths (826 mm) cans and two half-length cans (413 mm). Each can is welded circumferentially to its neighbor(s), creating one continuous section. There are 4 circumferential welds in each section. Two thick flanges (with thickness equal to 38.4 mm) are connected to the tubes at each end.

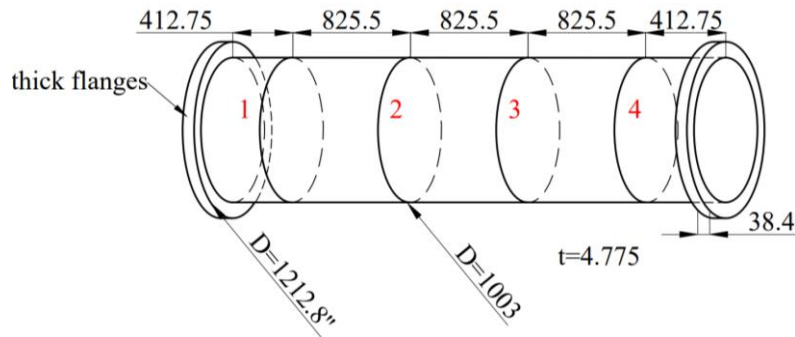
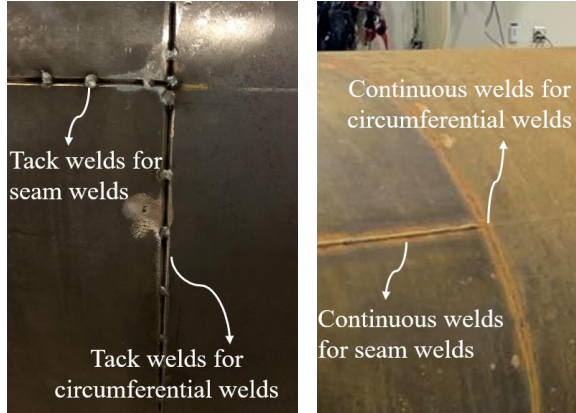


Fig 2: Nominal geometry of the tube sections considered in this paper, units in mm.

Both tubes were scanned twice: after tack welding (Fig.3 (a)) and after full continuous welding (Fig.3 (b)). The measured geometry of the tube sections after tack welding (i.e., before full circumferential welding) is referred to herein as the pre-welded geometry and the measured geometry after full circumferential welding is referred to herein as the post-welded geometry.

Measurements of these geometries utilize the same scanning setup and scanning procedure. As shown in Fig. 4, during scanning, the tube was placed on the ground, supported by the two thick end flanges, which elevate the bottom of the tube 105 mm above the ground. To capture the full-field geometric profile, four scans were conducted at four different locations. These four scans are sufficient to scan the entirety of the viewable surface of the tube sections with the maximum incident angle smaller than 70° , as mentioned in Section 2.2. Scanning locations are plotted in Fig. 5. As shown in this figure, for this set-up with the tube resting on the ground, there is an unscannable region of the tubes, comprising the bottom $\sim 60^\circ$ at the bottom of the tube as shown

in Fig. 5, causing missing data in the point cloud dataset for both the pre-welded and post-welded geometries. Note that the location of the unscannable region is different for these two geometries, because to weld the full circumferential welding, workers had to rotate the tube section by a certain degree around its longitudinal axis, and after that, the tube section rests on the ground in different position than where they were before full circumferential welding. In Section 4.2, this difference of the position of the unscannable region is illustrated with a dark blue block. The scanning process includes 18 white cube targets, which are used reference points to align different scan samples. The location of the targets was designed to ensure that there are at least six reference targets within the overlapping scanning area of two adjacent scans (e.g., scanner positions #1 and #2 in Fig. 5).



(a) tack weld (b) continuous weld
Fig 3: Details of tack weld and full continuous weld.

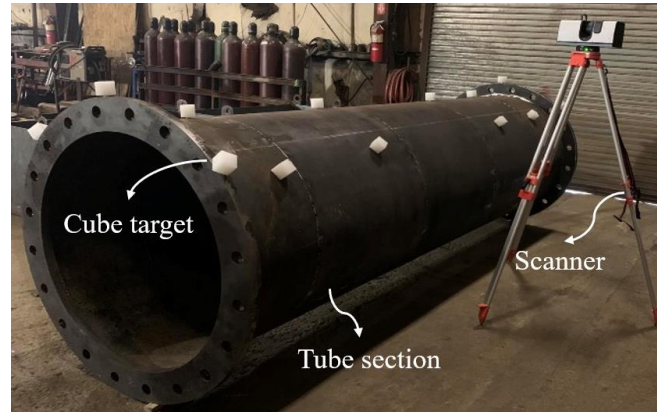
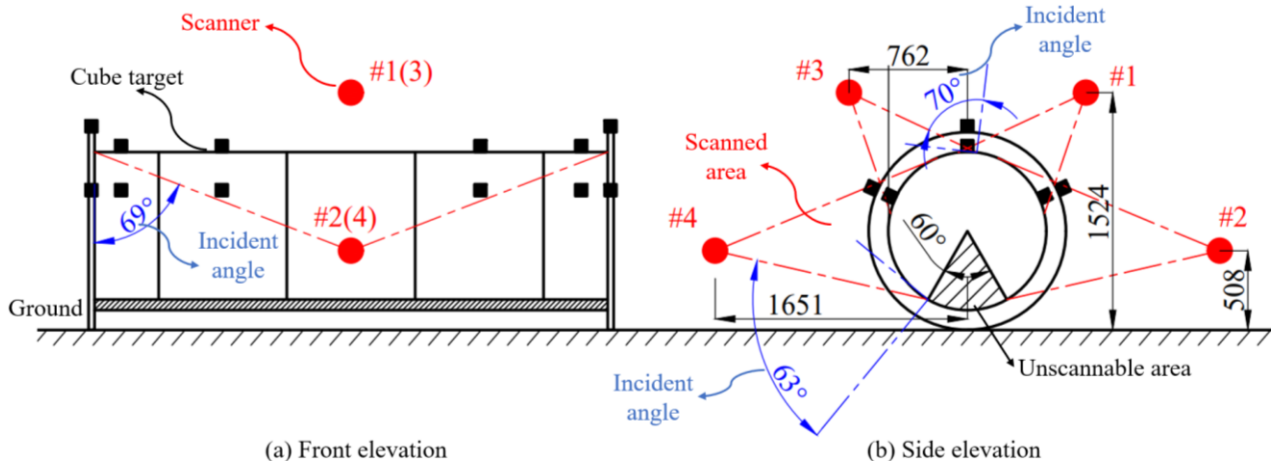


Fig 4: Picture of scanning setup.



(a) Front elevation (b) Side elevation
Fig 5: Illustration of the four scanner positions and 16 reference targets, unit in mm.

4. Geometric imperfections of the pre-welded and post-welded geometries

4.1 Data processing method to extract geometric imperfections

Geometric imperfections are calculated from the raw scan data using the following process. First, multiple scan samples are imported into Artec Studio, a commercially available point cloud analysis software provided by the scanner manufacturer. Alignment of these scan samples is conducted in the same software with an algorithm that uses pairs of point sets (i.e., cube targets) to detect scan areas that should be aligned.

The reference geometry for calculation of imperfections is selected using a numerical analysis to investigate the influence of gravity deformations. This revealed that the gravity deformations are negligible compared to the magnitude of measured imperfections. Therefore, the nominal geometry of the tube sections based on their drawings is selected as the reference geometry. The reference geometry is a structured point cloud with a resolution of 1mm both longitudinally and circumferentially. Radial deviations between the measured geometry and the reference geometry are calculated using point clouds of the two geometries that are aligned using the “Iterative Closest Point” (ICP) Algorithm (Wang et al. 2017).

4.2 Results of geometric imperfections

Fig. 6 shows the unrolled geometry of the tube sections. It defines terms and directions that are adopted in this paper. The x-axis represents the longitudinal position, and the y-axis represents the circumferential position ϕ , varying from $-\pi$ to π . Circumferential welds and seam welds are identified by black dashed lines. A grey block indicates positions on the tube surface that are within a distance λ away from the axis of seam welds at both sides, where $\lambda = 2.44\sqrt{Rt}$, the buckling half-wavelength for a tube in compression. The seam weld disrupts the shape of the weld depression, so scan data within the grey block is removed from the results.

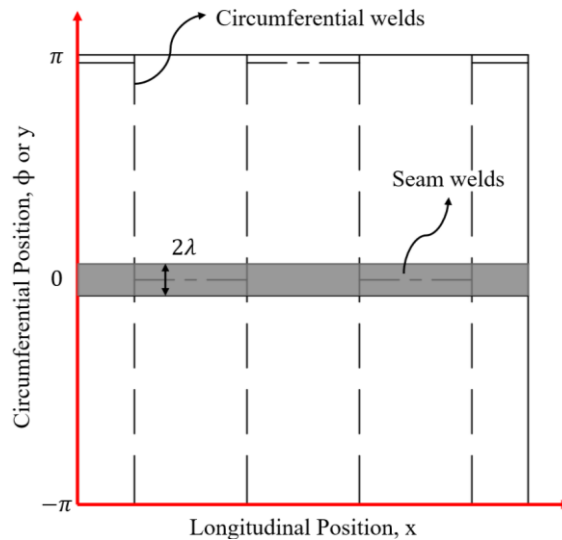


Fig 6: Schematic of the measured tube sections indicating

Fig. 7 and Fig. 8 show the measured geometric imperfections of Section-A and Section B, plotted with a common color scale. Color in the figure represents the magnitude of the radial imperfection with a positive value indicating an outward imperfection (i.e., with a radius greater than the reference geometry), and a negative value representing an inward imperfection. The dark blue block in these plots indicates the unscannable area. The cube targets are visible as concentrated areas of red in the dataset.

Comparing Fig. 7 (a) and Fig. 7 (b), or Fig. 8 (a) and Fig. 8 (b), it can be found that, the pre-welded geometry and the post-welded geometry share common imperfection patterns. For example, for Section-A, for the region between $x=1500\sim 2000$ and $\phi=0$, the pre-welded geometry and the post-welded geometry both have significant outward imperfections, and for the region between $x=2000\sim 2500$ and $\phi=-1$, they both have significant inward imperfections. Moreover, as a general

trend, imperfections of the pre-welded geometry tend to be larger than imperfections of the post-welded geometry. The reason for this is not yet clear.

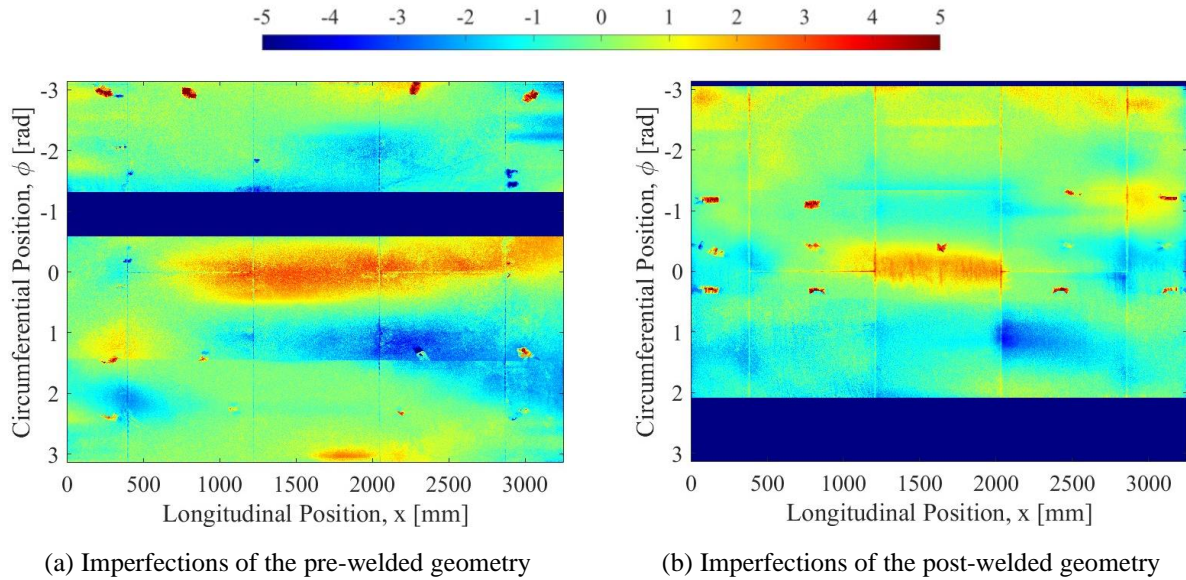


Fig 7: Geometric imperfections of Section-A.

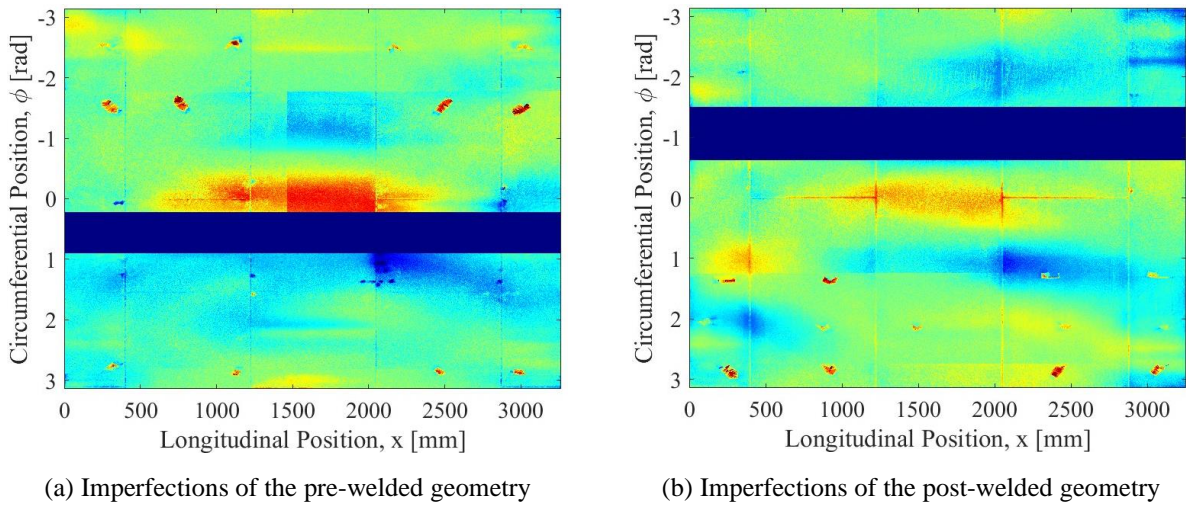


Fig 8: Geometric imperfections of Section-B.

5. Analysis of weld depression profile

5.1 Isolation method of weld depression profile

The focus of this paper is the difference in the local imperfections caused by full circumferential welding between the pre-welded geometry and the post-welded geometry. To investigate the evolution of geometric imperfections during fabrication, the average of the geometric imperfections adjacent to the circumferential welds before and after circumferential welding is calculated.

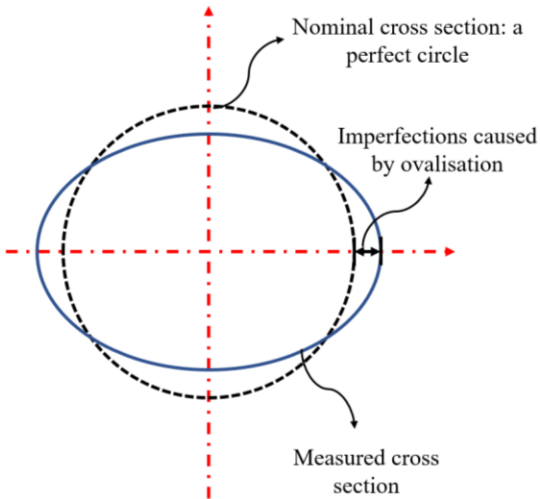


Fig 9: Illustration of imperfections caused by cross sectional ovalisation.

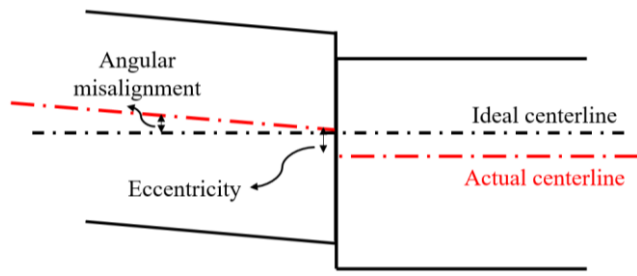


Fig 10: Illustration of imperfections caused by misalignment.

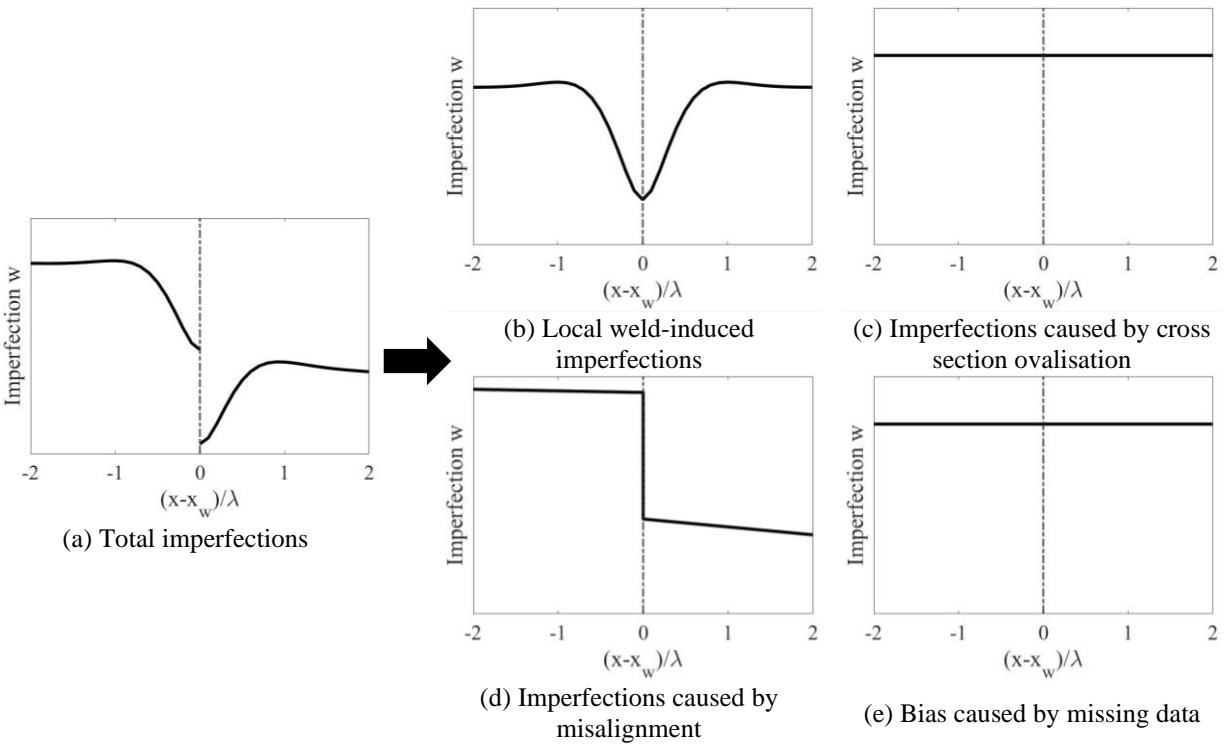


Fig 11: Illustration of imperfections close to circumferential welds.

The average of the overall imperfections can be considered as the sum of global imperfections (e.g., cross-section ovalisation, see Fig. 9), local imperfections, imperfections caused by misalignment between adjacent cans, bias caused by missing data within the unscannable region, and random imperfections that exist in the raw plates. Misalignment between adjacent cans causes an eccentricity and an angular misalignment, as illustrated in Fig. 10. Local imperfections (e.g., dimples) can be categorized into two types based on their directions: longitudinal dimples and circumferential dimples. The weld depression is one type of longitudinal dimple. The intent of this paper is to study the effect of weld depressions in isolation. To this end, global

imperfections, imperfections caused by misalignment between adjacent cans, and bias caused by missing data within the unscannable region are removed from the data. To do this, the total imperfections are decomposed into four parts, see Fig. 11. Global imperfections are represented as a constant, see Fig. 11(c). The average of misalignment between cans is represented by straight lines, see Fig. 11(d). Bias in the data is represented as a constant, see Fig. 11(e).

Following this process, the local weld-induced imperfections are isolated by fitting two independent lines to a region located between 1λ and 2λ from the weld on each side of the weld. Fig. 12 illustrates this method. The blue dashed line shows the average of the total imperfections; the blue solid line shows the average of the isolated weld-induced imperfections. Dashed black lines represent the fitted straight lines, representing the combination of imperfections caused by cross sectional ovalisation, imperfections caused by misalignments, and bias caused by missing data.

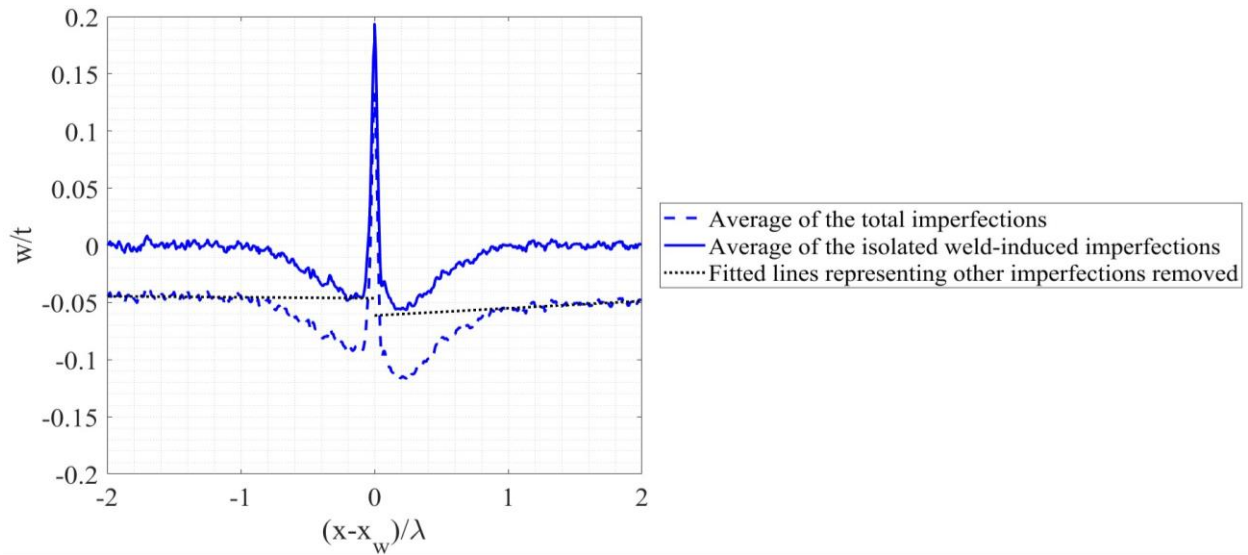


Fig 12: Example of the method for isolating local weld-induced imperfections.

5.2 Comparison of weld depression profile

Using the isolation method described above, a comparison of weld depression profiles between the pre-welded geometry and the post-welded geometry for Section-A and Section-B is plotted in Fig.13 and Fig. 14, respectively. The measured imperfection w is normalized by the thickness of the tube section t and the longitudinal position x is normalized by $\lambda = 2.44\sqrt{Rt}$. The data used to calculate the average profiles in Fig.13 and Fig.14 is intended to represent profiles that are not influenced by the seam weld, so the data in the averaging calculation only includes meridians that are spaced more than λ from the axis of the seam weld (i.e., meridians outside the shaded area around the axis of the seam weld in Fig. 6).

In each plot, the dashed red line and the red solid line show the average of the total imperfections and the isolated weld-induced imperfections of the pre-welded geometry. Similarly, the dashed blue line and the solid blue line show the average of the total imperfections and the isolated weld-induced imperfections of the post-welded geometry. The solid black line and the dotted black line represent the R&T model profile corresponding to $\xi=1$ and $\xi=0$, respectively, shown for an

example imperfection amplitude of $0.06t$. The shaded gray area indicates the range affected by the weld bead or scan inaccuracies due to sharp edges at the weld centerline.

These plots show that the profiles of the post-welded geometry exhibit geometrically similar features with a similar geometry as the R&T profile with $\xi=1$, while the profiles of the pre-welded geometry have no obvious patterns. That is because the former is dominated by the inward circumferential welds, and the latter mainly reflects random imperfections in the raw plate and imperfections from rolling of the plates. For both sections, the weld depression profiles of the post-welded geometry of all welds show clear symmetry, except for Weld #1 in Section-A (Fig. 13 (a)). The plots also show that the maximum value of the depression varies from approximately $0.04t$ to $0.08t$.

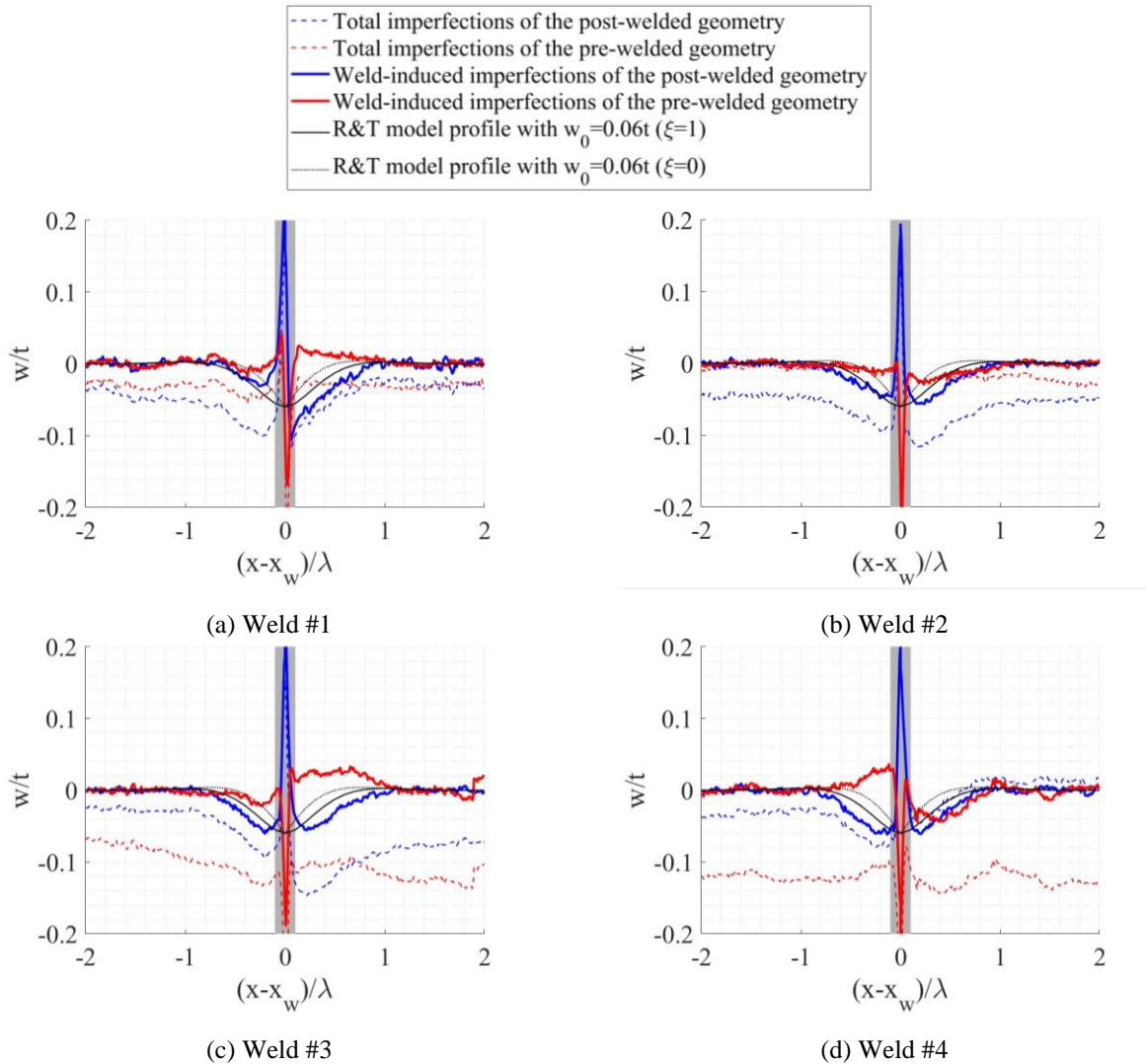


Fig 13: Comparison of average weld depression profile between the pre- and post- welded geometries for Section-A.

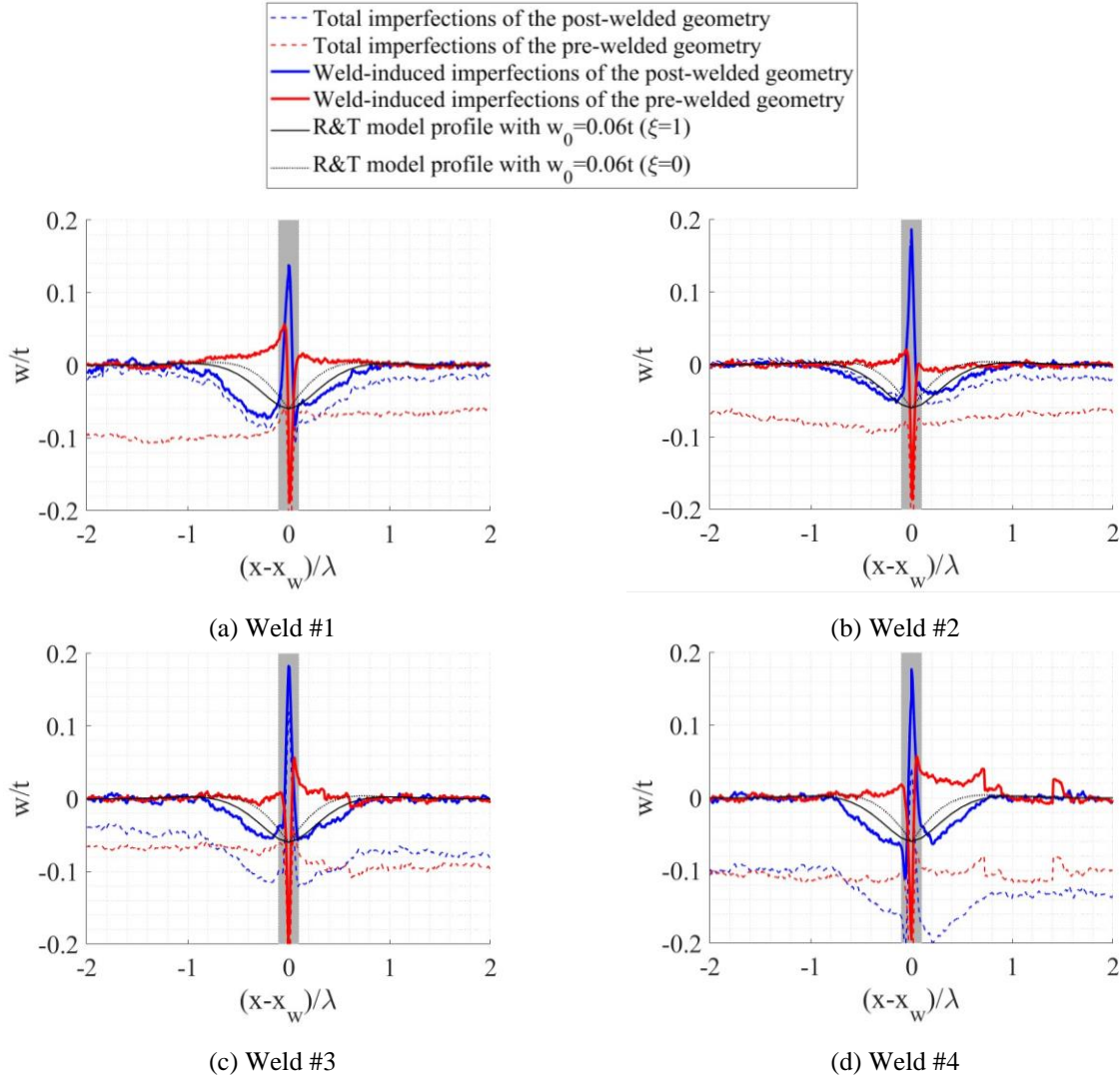


Fig 14: Comparison of average weld depression profile between the pre- and post-welded geometries for Section-B.

Fig. 15 compares the profiles of weld depression near and away from the seam weld axis. The blue solid lines represent the profile of meridians more than λ from the seam weld axis (outside the gray shaded area in Fig. 6) for the post-welded geometry, while the red dotted lines represent the profile of meridians less than λ from the axis (inside the gray shaded area in Fig. 6) for the post-welded geometry.

The comparison shows that the profiles near the seam weld axis have a much higher degree of variation compared to the profiles further away, and display no clear indication of an inward weld depression. The profiles near the seam weld axis are largely impacted by the seam weld, such as the weld bead. This high degree of variation highlights the need to exclude these profiles from future calculations of weld depression.

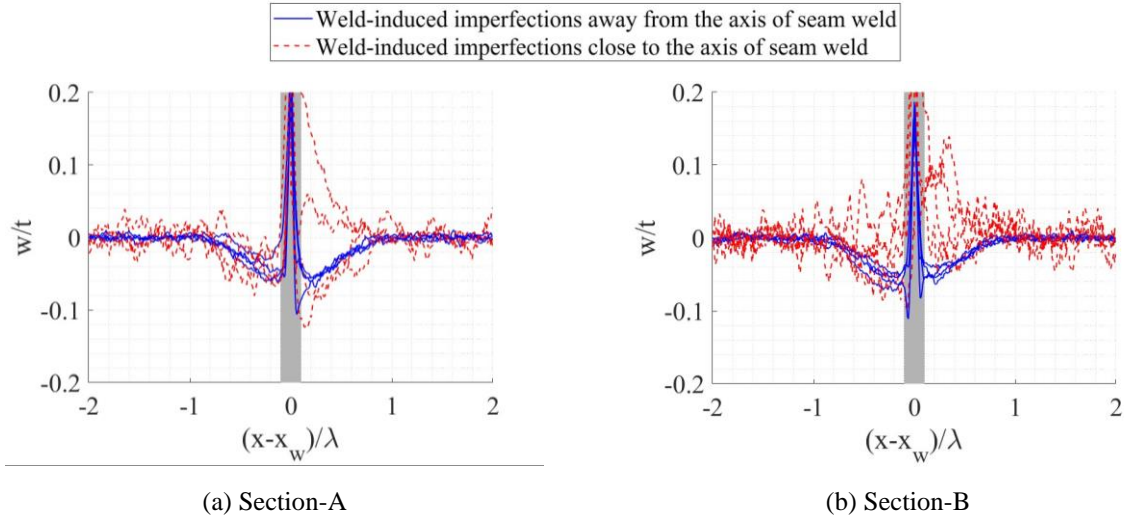


Fig 15: Average weld depression profiles of the post-welded geometry at locations closer to and farther than λ from the axis of the seam weld.

4. Conclusions

Geometric imperfections of two can-welded thin-walled tube sections before and after circumferential welding are identified and analyzed based on high-resolution measurements using a 3D laser scanner. After removing the influence of imperfections caused by cross section ovalisation, misalignments, and missing data, the post-welded measurements show a consistent inward weld depression profile at circumferential weld locations spaced farther than 1λ away from the axis of the seam weld, where λ is the buckling half-wavelength of the tube in bending. A consistent profile is not observed for the pre-welded measurements. The maximum depressions of the post-welded geometry vary from approximately $0.04t$ to $0.08t$. For imperfection profiles spaced closer than 1λ from the axis of seam weld, the imperfection profiles have large variations and lack a consistent pattern.

Acknowledgments

The authors gratefully acknowledge the financial support of the US National Science Foundation through award #1912354 and award #1912481. Any opinions, findings, and conclusions or recommendations expressed in this material are those of the authors and do not necessarily reflect the views of the National Science Foundation. The assistance of Michael MacNeil and Nicholas Briggs at Northeastern University is greatly appreciated.

References

- Rotter, J.M., Teng, J.G. (1989). "Elastic stability of cylindrical shells with weld depressions." *Journal of Structural Engineering*, 115 (5) 1244–1263.
- White, J.D., Dwight, J.B. (1977). "Weld shrinkage in large stiffened tubulars." *Proceedings of a Conference on Residual Stresses in Welded Constructions*, London, UK. 37–48.
- Pircher, M., Berry, P. A., Ding, X., Bridge, R. Q. (2001). "The shape of circumferential weld-induced imperfections in thin-walled steel silos and tanks." *Thin-Walled Structures*, 39(12), 999-1014.
- Sadowski, A. J., Van Es, S. H. J., Reinke, T., Rotter, J. M., Gresnigt, A.M. (Nol), Ummenhofer, T. (2015). "Harmonic analysis of measured initial geometric imperfections in large spiral welded carbon steel tubes." *Engineering Structures*, 85, 234-249.
- Soudarissanane, S., Lindenbergh, R., Menenti, M., Teunissen, P. (2011). "Scanning geometry: Influencing factor on the quality of terrestrial laser scanning points." *ISPRS journal of photogrammetry and remote sensing*, 66(4), 389-399.

- Lichti, D. D. (2007). "Error modelling, calibration and analysis of an AM–CW terrestrial laser scanner system." *ISPRS journal of photogrammetry and remote sensing*, 61(5), 307-324.
- Guo, J., Wang, Q., Park, J. H. (2020). "Geometric quality inspection of prefabricated MEP modules with 3D laser scanning." *Automation in Construction*, 111, 103053.
- Selvaraj, S., Madhavan, M. (2018). "Geometric imperfection measurements and validations on cold-formed steel channels using 3D noncontact laser scanner." *Journal of Structural Engineering*, 144(3), 04018010.
- Kainat, M., Adeeb, S., Cheng, J. R., Ferguson, J., Martens, M. (2012). "Identifying initial imperfection patterns of energy pipes using a 3D laser scanner." *International Pipeline Conference*, 45134, 57-63.
- Mirzaie, F., Myers, A. T., Jay, A., Mahmoud, A., Smith, E., Schafer, B. W. (2020). "Analysis of geometric imperfections of spirally welded slender steel tubes." *Thin-Walled Structures*, 146, 106447.
- Wang, F., Zhao, Z. (2017). "A survey of iterative closest point algorithm." *Chinese Automation Congress (CAC)*, pp. 4395-4399.